Contents lists available at ScienceDirect

Atmospheric Research

journal homepage: http://ees.elsevier.com

Multi-sensor observations of an elevated rotor during a mountain wave event in the Eastern Pyrenees

Mireia Udina [a,*], Joan Bech [a], Sergi Gonzalez [a,b], Maria Rosa Soler [a], Alexandre Paci [c], Josep Ramón Miró [d], Laura Trapero [e], Jean Marie Donier [c], Thierry Douffet [c], Bernat Codina [a], Nicolau Pineda [d]

[a] Departament de Física Aplicada – Meteorologia, Universitat de Barcelona, C/Martí i, Franquès, 1, 08028 Barcelona, Spain
[b] DT Catalonia, Agencia Estatal de Meteorologia (AEMET), Barcelona, Spain
[c] CNRM, UMR3589 METEO-FRANCE and CNRS, 31100 Toulouse, France
[d] Department of Territory and Sustainability, Meteorological Service of Catalonia, Generalitat de Catalunya, Barcelona, Spain
[e] Snow and Mountain Research Center of Andorra (CENMA-IEA), Institut d'Estudis, Andorrans, Av. Rocafort, 21-23, Sant Julià de Lòria AD600, Andorra

ARTICLE INFO

Keywords
Mountain waves
Rotor
Turbulence
Winter storm
Eastern Pyrenees
Cerdanya

ABSTRACT

The 15 January 2017 a strong northerly synoptic flow lead to the generation of mountain waves and heavy snowfall over the eastern Pyrenees, particularly over the Cerdanya valley near the border between France, Spain and Andorra. Measurements from several instruments deployed during the Cerdanya-2017 field campaign and satellite imagery revealed the presence of mountain waves and the formation of an associated rotor underneath the first mountain wave crest. The evolution and location of the mountain waves were studied using high temporal resolution data from a UHF wind-profiler and a vertically pointing K-band Doppler radar, separated a few kilometres in horizontal distance. A mountain wave with a wavelength about 18 km was detected in the morning and shortened slightly in the afternoon when a transient rotor, elevated approximately 140 m above the ground, was formed, disconnected from the surface flow. A strong turbulence zone was identified at the upper edge of the mountain wave, above the rotor, a feature observed in previous studies. The mountain wave and rotor induced circulation was favoured by the valley shape and the second mountain ridge location, in addition to the weak and variable winds, established during the sunset close to the valley surface.

1. Introduction

An atmospheric rotor can be defined as a low-level turbulent closed flow located underneath a mountain wave crest with a circulation horizontal axis oriented parallel to the mountain ridge (Kuettner, 1938; Doyle and Durran, 2002). The formation of a rotor is tied to the presence of stationary gravity waves at the lee of a mountain, generated when the air parcels are excited by the mountain obstacle in a stably stratified flow. Rotors can lead to severe turbulence and pose a hazard for the aeronautical activity at the lower troposphere near mountain ranges (e.g. Darby and Poulos (2006); Schneider et al. (2017)) The strong turbulence and wind shear within the rotors represent a danger particularly for the glider community. For example, in 1955 during the Jet Stream Project Holmboe and Klieforth (1957) a research glider was destroyed by a rotor. However, gliders may also take profit of the ascending part of the rotor in order to get elevated and reach the laminar flow (see for example Worthington (2017)).

Different types of rotors have been documented using observations and have been reproduced in idealised numerical simulations. Hertenstein and Kuettner (2005) described two types of rotors in idealised and simplified numerical simulations: (i) a frequent rotor formed under resonant mountain wave crests and (ii) a much more turbulent and less frequent rotor formed in association with hydraulic jumps and downslope windstorms. Other observations and idealised simulations highlighted the importance of elevated temperature inversion on rotor formation (Vosper, 2004; Mobbs et al., 2005). Later, Doyle and Durran (2007) analysed the internal structure of rotors through 2D and 3D large-eddy simulation (LES), revealing differences in the detailed subrotor structures along the vortex sheet lifted by the lee-waves. However, recent studies have proved that a wider variety of turbulent flow structures similar to a rotor can exist (Strauss et al., 2016) and their generation can be highly transient and intermittent (Kühnlein et al., 2013), substantially modifying the idealised two-dimensional structure of a rotor described in previous studies.

* Corresponding author.
E-mail address: mudina@meteo.ub.edu (M. Udina)

https://doi.org/10.1016/j.atmosres.2019.104698
Received 12 March 2019; Received in revised form 26 September 2019; Accepted 29 September 2019
Available online xxx
0169-8095/

In addition, the atmospheric boundary layer (ABL) structure highly influences the rotor characteristics and vice-versa. In this way, wave-induced boundary layer separation with adverse pressure gradients leads to formation of atmospheric rotors (Doyle and Durran, 2002) while the ABL thickness and evolution highly depends on the wave features, such as the wave length, amplitude and phase (Jiang et al., 2006; Smith et al., 2006; Smith, 2007), which modulates the characteristics of the rotor. Besides, the presence of a second ridge may interfere the lee-wave and impact the rotor formation (Grubišic and Stiperski, 2009; Stiperski and Grubišic, 2011). In recent theoretical studies non-hydrostatic effects seem to be essential for rotor formation (Sachsperger et al., 2016). On the other hand, despite many studies have showed the effect of the orographic induced vertical motions in precipitation enhancement (e.g. Houze Jr. (2012); Trapero et al. (2013a, 2013b); de la Torre et al. (2015)) only a few have examined the interaction between winter storm mountain-wave kinematic structures and orographic precipitation (Kingsmill et al., 2016; Valenzuela and Kingsmill, 2017, 2018) or Gonzalez et al. (2019), who reported a decoupling between surface precipitation and orographically induced circulations during the event analysed in the present paper.

Several field studies have been carried out in the last decades in order to study mountain waves and their associated processes. In Europe, the Alpine Experiment (ALPEX) in the 1980s (Hoinka, 1984, 1986), the PYREX experiment in the northern side Pyrenees (Bougeault et al., 1990, 1997) in the 1990s, and more recently the Mesoscale Alpine Experiment (MAP; Bougeault et al. (2001); Smith et al. (2007)) over the Alps studying strong winds and föhn events (Gohm and Mayr, 2004; Guéenard et al., 2006). However, fewer observational campaigns have focused specifically on atmospheric rotors. The first relevant exploration of rotor structures was the Sierra Wave Project conducted in the early 1950s in the lee of Sierra Nevada (USA) as described in Grubišic and Lewis (2004). In the same location but several years later, the Terrain-Induced Rotor Experiment (T-REX; Grubišić et al. (2008)) became a great success to improve the understanding of the rotor structures and evolution, as well as the interaction among mountain waves, rotors and boundary layer. Recent research dealing with atmospheric rotors have studied bora wind events (Gohm et al., 2008) or strong winds in Iceland (Ágústsson and Ólafsson, 2014), mainly reproduced by numerical simulation but with limited observation datasets. In addition, a few laboratory experiments have also focused on this topic (Knigge et al., 2010; Stiperski et al., 2017).

In this work we present the results of a mountain wave event and an associated rotor observed during a winter storm heavy snowfall in the course of the Cerdanya-2017 field experiment conducted over the eastern Pyrenees, in Cerdanya basin (Fig. 1), between Occitaine (France) and Catalonia (Spain). The field campaign target studies were based on previous research in the area and were the following: a) cold-air pool formation and local wind circulation under stable conditions (Miró et al., 2017; Jiménez-Esteve et al., 2018; Conangla et al., 2018); b) mountain wave, rotors, and low-level turbulence (Udina et al., 2017) and c) orographic effects on precipitation processes (Trapero et al., 2013b). The study presented here, mainly based in remote sensing observations, corresponds to the second part and the main objectives are: (i) to document the formation of a rotor underneath a mountain wave generated on the Eastern Pyrenees during a snowfall episode; (ii) to characterise the conditions for a rotor formation and determine the changes in the flow dynamics induced by the presence of the rotor; (iii) to estimate the structure of the rotor (horizontal and vertical extension) also identifying turbulent areas.

The paper is organised as follows. Section 2 introduces the geographical location and the observing systems in the Cerdanya-2017 field experiment. Section 3 provides an overview of the mountain waves and precipitation distribution of the event, from synoptic to local scale. Section 4 presents the field experiment observations relevant for the rotor analysis. Section 5 discusses the main characteristics and evolution of the mountain waves and the rotor. Finally, conclusions and final remarks are given in Section 6.

2. The Cerdanya-2017 field campaign

2.1. Geographical location

The Pyrenees mountain massif is a west to east oriented mountain range located in southwest Europe along the border between France and Spain (Fig. 1). In the Eastern Pyrenees the Cerdanya basin (hereafter Cerdanya valley) sits around 1000 m above sea level (ASL) and, unlike most of the Pyrenean valleys, it is oriented from ENE to WSW, nearly parallel to the mountain ranges (Fig. 1). The main study area is approximately a flat bottomed 10 km × 30 km rectangle and it is surrounded by mountain ranges with summits exceeding 2900 m ASL: Carlit (2921 m) and Puigpedrós (2914 m) at the north side, Cadí and Moixeró sub-ranges (peaking at 2649 m) at the south side, and the Puigmal (2910 m) at the southeast (Fig. 1a). The main measurement site of the Cerdanya-2017 field campaign was deployed at the centre of the basin, in the Cerdanya Aerodrome (A in Fig. 1). This site, located at 1095 m ASL, is a facility well known for the gliding community (ICAO code LECD).

Due to the geographical location of the basin, very strong winds occur with northerly synoptic flows, especially during winter when the synoptic configuration favours strong northerly advections (Esteban et al., 2005; Lemus-Canovas et al., 2019). After crossing the first mountain range of the Pyrenees, mountain waves are likely to be generated in stably stratified atmospheric layers and therefore rotors are also likely to be formed in association with these mountain waves over the Cerdanya valley (Udina et al., 2017). The presence of a secondary and lower mountain ridge at the south may influence the mountain wave phase and the rotor structure underneath, as discussed in Stiperski and Grubišic (2011) using idealised numerical experiments and observed in Stiperski et al. (2017) in the laboratory experiments.

2.2. Observing network

The Cerdanya-2017 field experiment took place in this valley from October 2016 to May 2017. It was a joint effort of several teams from the Euroregion Pyrenees-Mediterranean, that belong mainly to the University of Barcelona, the University of the Balearic Islands, METEO-FRANCE and the Meteorological Service of Catalonia.

The main instrumented site was located at the aerodrome (A) (see scheme of Fig. 2) with several instruments continuously measuring profiles of different meteorological variables. For the present study we will use the Micro Rain Radar (MRR), the scanning Doppler wind lidar (LIDAR), the Wind RASS-Sodar (WR), the Automatic Weather Station (AWS) and the Atmospheric soundings (RS) launched for specific periods during the field experiment, all of them located at A. Among the other instruments deployed in the area during this field experiment, we will present measurements from a Ultra-High Frequency wind profiler (UHF) radar located a few km to the NW from the A site and an AWS, number 8, located very close the UHF (see Fig. 1). Table 1 summarises the instruments and some of their characteristics.

The UHF wind profiler radar, model Degréane PCL 1300, was located in the village of All about 2.4 km North from the main site, at 1077 m ASL. Radio waves were emitted and received by 5 antennas in the following directions: vertical, north, east, south and west at a frequency of 1274 MHz. The UHF radio waves are mainly backscattered by the fluctuations of the air refractive index (induced by the fluctuations of air temperature and humidity), providing measurements of the wind profile up to about 3–4 km above ground level (AGL) from the

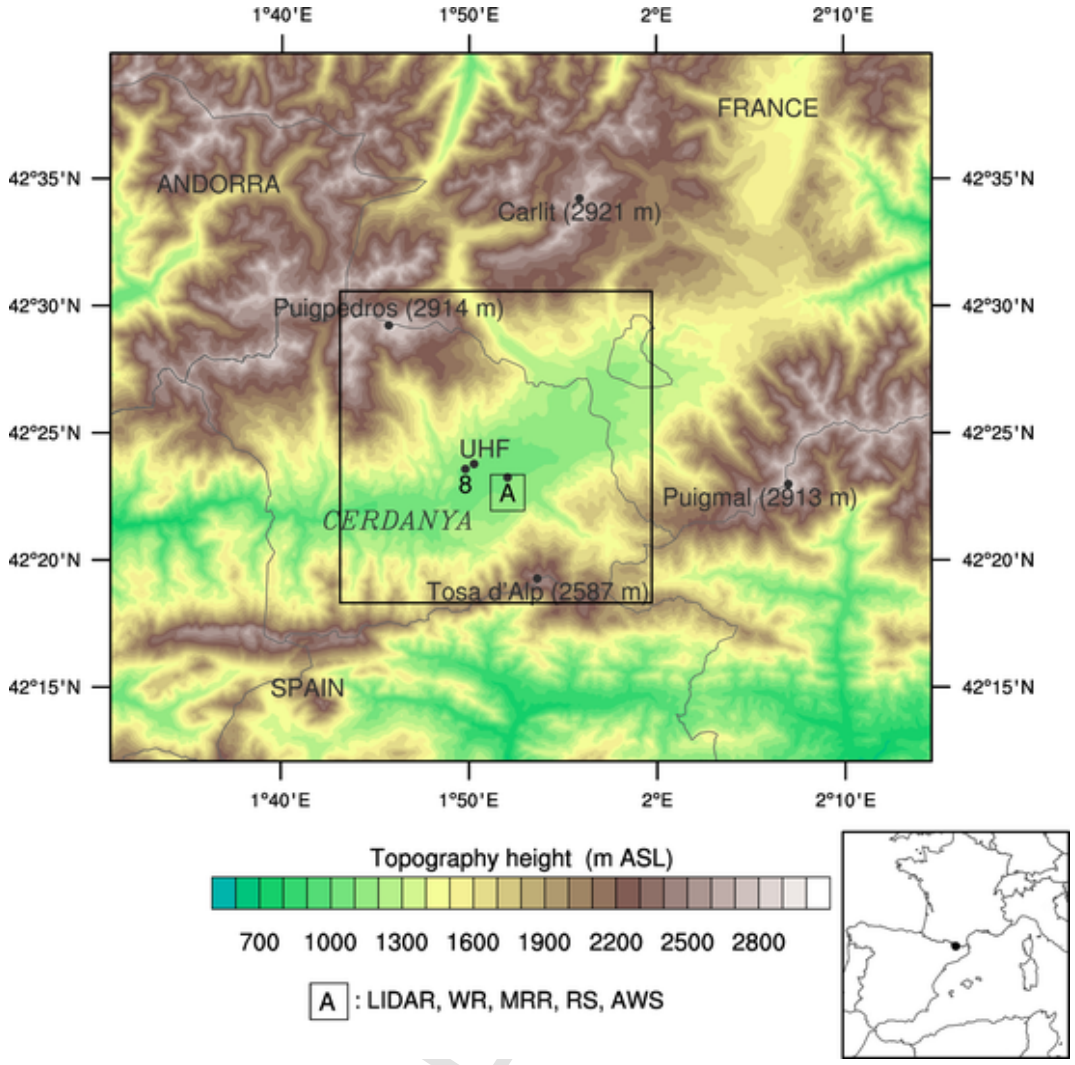

Fig. 1. Topography of the Eastern Pyrenees region of study showing the location of the aerodrome (A) with most of the instrumentation: Micro Rain Radar (MRR), scanning Doppler wind lidar (LIDAR), Wind Radio Acoustic Sounding System (WR), atmospheric soundings (RS) and an automatic weather surface station (AWS); location of and additional AWS (number 8) and the Ultra-High Frequency wind profiler (UHF). The main mountain peaks of Carlit (2921 m ASL), Puigpedrós (2914 m ASL) and Puigmal (2913 m ASL) are also labelled, as well as Andorra, France and Spain and their borders. The black square corresponds to the zoomed area in Fig. 2a. The large scale location of the Pyrenees and the studied area is marked with a black point at the right bottom corner of the figure.

Doppler shift. The radio waves are not attenuated by rain and clouds at this frequency, so measurements are reliable under all sky conditions. For the analysed episode we use an acquisition mode data which provides a profile of the three wind components every 3–4 min with a vertical resolution of 100 m, up to 4000 m.

The Doppler wind lidar (LIDAR), model Leosphere WLS200S, was installed at the top of the aerodrome control tower about 10 m above the ground level, at 1110 m ASL. This instrument has been previously used in an alpine valley where it provided very useful information on the fine scale wind dynamics within the valley (Paci et al., 2016; Sabatier et al., 2018). During the Cerdanya-2017 field experiment, the scanning cycle was composed of a quasi-horizontal plan (Plan Position Indicator, PPI) and four vertical plans (Range Height Indicator, RHI) every 10 min, one of them oriented to the UHF location.

The Micro Rain Radar (MRR), a 24-GHz (K-band) radar manufactured by Metek (Löffler-Mang et al., 1999), is a portable Doppler weather radar vertical profiler that operates using a FM-CW (Frequency Modulated Continuous Wave) scheme. The instrument has a sampling frequency of 10 s. The Doppler spectra is divided into 64 bins from 0 to 12 m s^{-1} over 32 range gate bins. A vertical resolution of 100 m was selected for this study providing precipitation measurements from 300 to 3000 m AGL since the first two gates and the last one are affected by near-field effects and noise respectively. The manufacturer processing software assumes that vertical velocities of precipitation particles are only positive (i.e. falling hydrometeors) from 0 to 12 m s^{-1}. This assumption may lead to errors during convective showers (Tridon et al., 2011; Adirosi et al., 2016) and, particularly relevant for this study, in upward air movements with embedded snow particles. To avoid this problem, we used the processing developed by Maahn and Kollias (2012) that improves the system sensitivity for solid precipitation and allows to detect upward movements of the particles. The MRR allows us to monitor the precipitation variability and the vertical movements assuming that it is the resulting of overlap the falling velocity of the snow particles and the vertical velocity of the wind. The MRR was located at the aerodrome at 1099 m ASL, separated 2.4 km in linear distance from the UHF location (see Fig. 1), therefore data from both instruments could be readily compared and provide a complementary view of existing mountain waves over the area. In order to complete the precipitation features at the surface we used an optical disdrometer Parsivel (Löffler-Mang and Joss, 2000) located next to the MRR, which provides the size and velocity distribution of the precipitation particles.

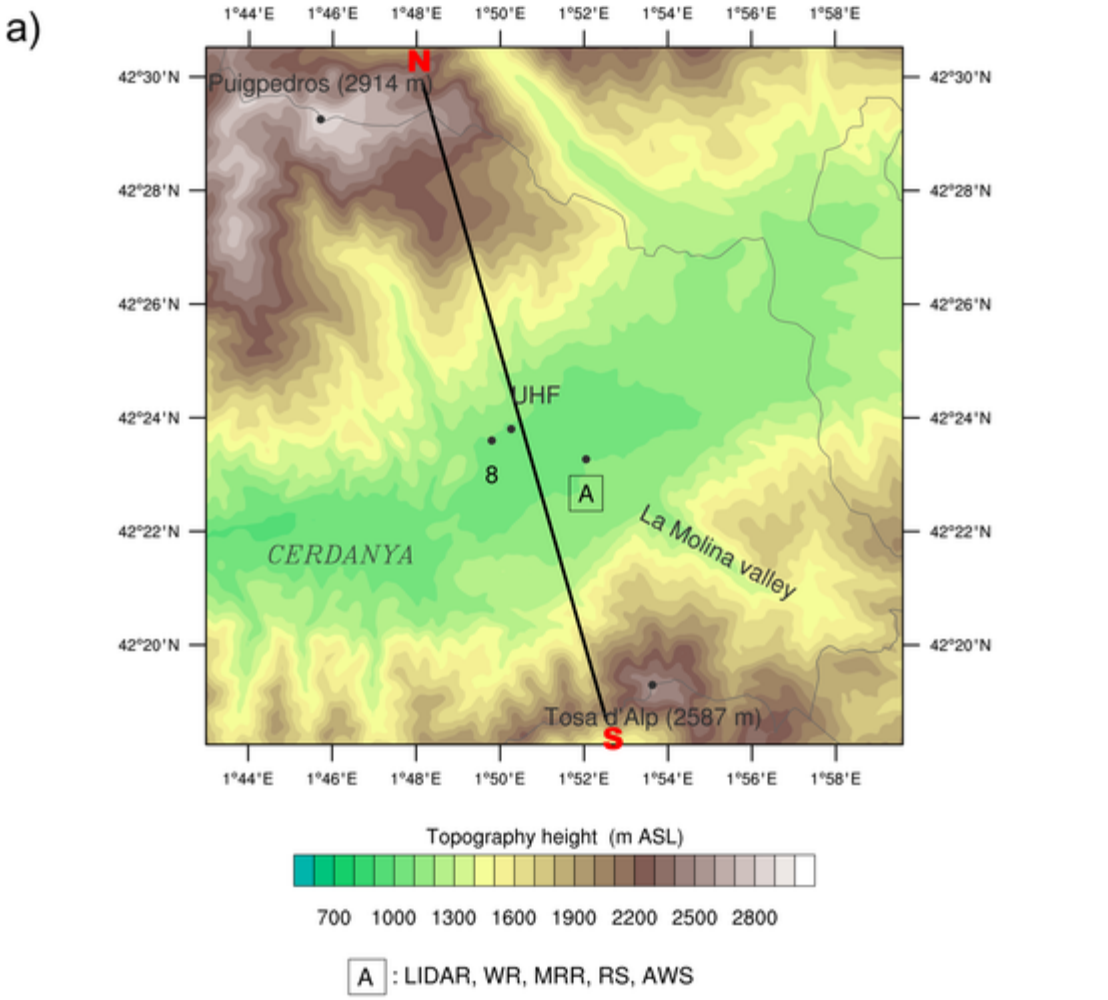
a)
1°44'E
1°46'E
1°48'E
1°50'E
1°52'E
1°54'E
1°56'E
1°58'E
42°30'N
42°28'N
42°26'N
42°24'N
42°22'N
42°20'N
N
S
Puigpedros (2914 m)
UHF
8
A
CERDANYA
La Molina valley
Tosa d'Alp (2587 m)
Topography height (m ASL)
700 1000 1300 1600 1900 2200 2500 2800
A : LIDAR, WR, MRR, RS, AWS

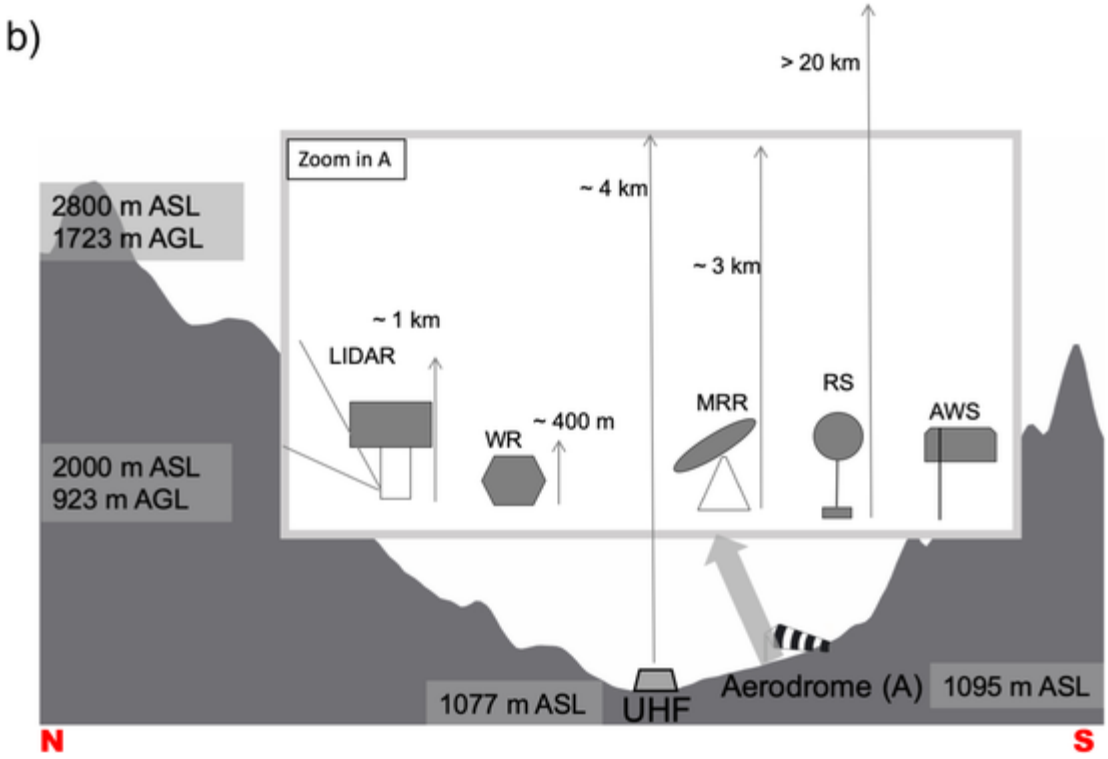
b)
> 20 km
Zoom in A
~ 4 km
~ 3 km
~ 1 km
LIDAR
WR
~ 400 m
MRR
RS
AWS
2800 m ASL
1723 m AGL
2000 m ASL
923 m AGL
1077 m ASL
UHF
Aerodrome (A)
1095 m ASL
N
S

Fig. 2. a) Zoomed topography of the region of study with a black line corresponding to the cross section used for the terrain elevation in panel b) with the north (N) and south (S) limits labelled in red; b) schematic view of the instruments deployed in the Cerdanya valley with their vertical range, in the cross section following the line marked in panel a). At the mountain foot there is the Ultra-High Frequency wind profiler (UHF) and at the aerodrome (A) the following instruments: scanning Doppler wind lidar (LIDAR), Wind RASS-Sodar (WR), Micro Rain Radar (MRR), atmospheric soundings (RS) and an automatic weather surface station (AWS). The vertical range for the remote sensing instruments is indicated with grey arrows (Note that vertical ranges and horizontal distances are not to scale). (For interpretation of the references to colour in this figure legend, the reader is referred to the web version of this article.)

Table 1
Ground-based instruments used in this study from the Cerdanya-2017 field experiment, their abbreviation, location, measured parameters used in this study and sample rate. The measured parameters are: horizontal wind components (u, v), vertical wind component (w), turbulent kinetic energy dissipation rate (ε), radar reflectivity (Z), virtual temperature (T_v), air temperature (T), relative humidity (RH), atmospheric pressure (P). Note that unlike the UHF, MRR w records correspond to hydrometeors and not to the vertical wind component.

Instrument	Abbrev.	Location	Coordinates	Parameters	Sample rate
Ultra-high frequency wind profiler	UHF	Mountain foot	42.3968 N, 1.8377 E	u, v, w, ε	3–4 min
Doppler wind lidar	LIDAR	Aerodrome	42.3876 N, 1.8683 E	radial velocity	10 min
Micro rain radar	MRR	Aerodrome	42.3864 N, 1.8665 E	Z, w (hydro)	1 min
Wind RASS-Sodar	WR	Aerodrome	42.3862 N, 1.8667 E	T_v, u, v	15 min
Atmospheric sounding	RS	Aerodrome	42.3865 N, 1.8681 E	u, v, T, RH, P	2 s
Automatic weather station	AWS A	Aerodrome	42.3861 N, 1.8664 E	u, v, T, RH	1 min
Automatic weather station	AWS 8	Mountain foot	42.3934 N, 1.8298 E	u, v, T, RH	1 min

A Wind Radio Acoustic Sounding System (WR), or Wind RASS-Sodar manufactured by Sintec, was located at 1100 m ASL. These instruments provide virtual temperature profiles up to hundreds of meters by combining remote sensing of acoustic and radio waves which are emitted by an antenna in five directions (vertical, north, east, south and west) at 1290 MHz. In addition, the combined radio-acoustic measurement technique also provide wind measurements trough the spectral analysis of backscattered energy Doppler shift.

Finally two AWS were used, one located at the aerodrome (Fig. 1, label A), at 1097 m ASL, and another, so-called AWS number 8 (Fig. 1, label 8), located at 1088 m ASL.

3. Event overview

The 15 January 2017 event occurred during the Cerdanya- 2017 field campaign was characterized by strong winds, mountain waves and relevant snow accumulation over the Cerdanya valley and the eastern Pyrenees. In order to understand the general large scale features of the episode, we analyse the synoptic flow structure and the cloud and precipitation distribution through satellite imagery and radar products.

3.1. Large scale flow

On 15 January 2017 the Iberian Peninsula was affected by a strong northerly wind flowing at all tropospheric levels as a result of a wide geopotential trough located over the continent and a wide geopotential ridge located over the North Atlantic Ocean (Fig. 3). The flow was driven by a meridional branch of the polar jet with velocities over 40 m s^{-1} at 300 hPa flowing from northern Europe to Spain. This type of flow impinging perpendicularly to the Pyrenees, under stable stratification conditions, leads to the generation of mountain waves after

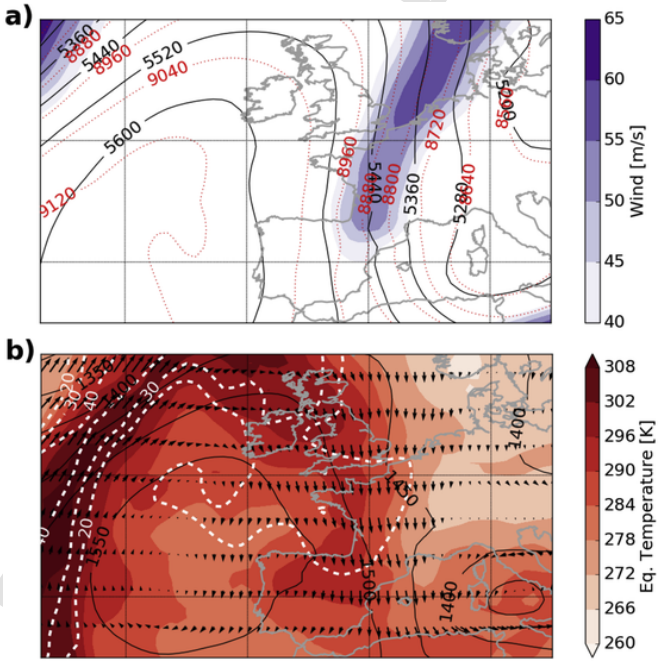

Fig. 3. ERA-Interim reanalysis on 15 January 2017 at 1800 UTC. a) Geopotential height (red dotted lines) and wind speed (shaded) at 300 hPa, and geopotential height (black lines) at 500 hPa. b) Geopotential height (black lines) and equivalent temperature (shaded) at 850 hPa, and wind (arrows) and specific humidity (white dashed lines) at 700 hPa. (For interpretation of the references to colour in this figure legend, the reader is referred to the web version of this article.)

crossing the mountain range, at its lee side. Between the trough and the ridge, a stationary baroclinic boundary associated to a strong horizontal gradient of equivalent temperature and consequently of symmetric instability (Kurz, 1998; Markowski and Richardson, 2011), produced abundant cloudiness at low levels over the British islands and France moving perpendicularly over the Pyrenees with the incident northerly wind (Fig. 3a). This long and thin structure, originated at sub-tropical latitudes, is also associated with large amounts of specific humidity at 700 hPa and indicates the presence of an atmospheric river (Fig. 3b). The atmospheric river remained almost stationary during the period between 15 and 16 January during which the descending branch of the ridge was gradually advecting relatively warm and moist air to the south. The episode ended when the jet moved east-wards and the oceanic relatively mild and moist air mass at low levels was replaced in the afternoon of 16 Jan 2017 by a continental cold and dry air mass coming from Central Europe due to a high-pressure wedge extension of the Atlantic anticyclone extending to north continental Europe and changing wind flow to a northeast circulation.

3.2. Spatial cloud and precipitation distribution

The Moderate Resolution Imaging Spectroradiometer (MODIS) Terra satellite crossed the area of study at 1035 UTC. Local time was one hour after UTC. Fig. 4a shows a 250 m resolution image combining bands 3, 6 and 7, where the land surface is enhanced using green colours, low level clouds are red and high clouds are white. We can distinguish two deep cloud bands oriented parallel to the mountain range,

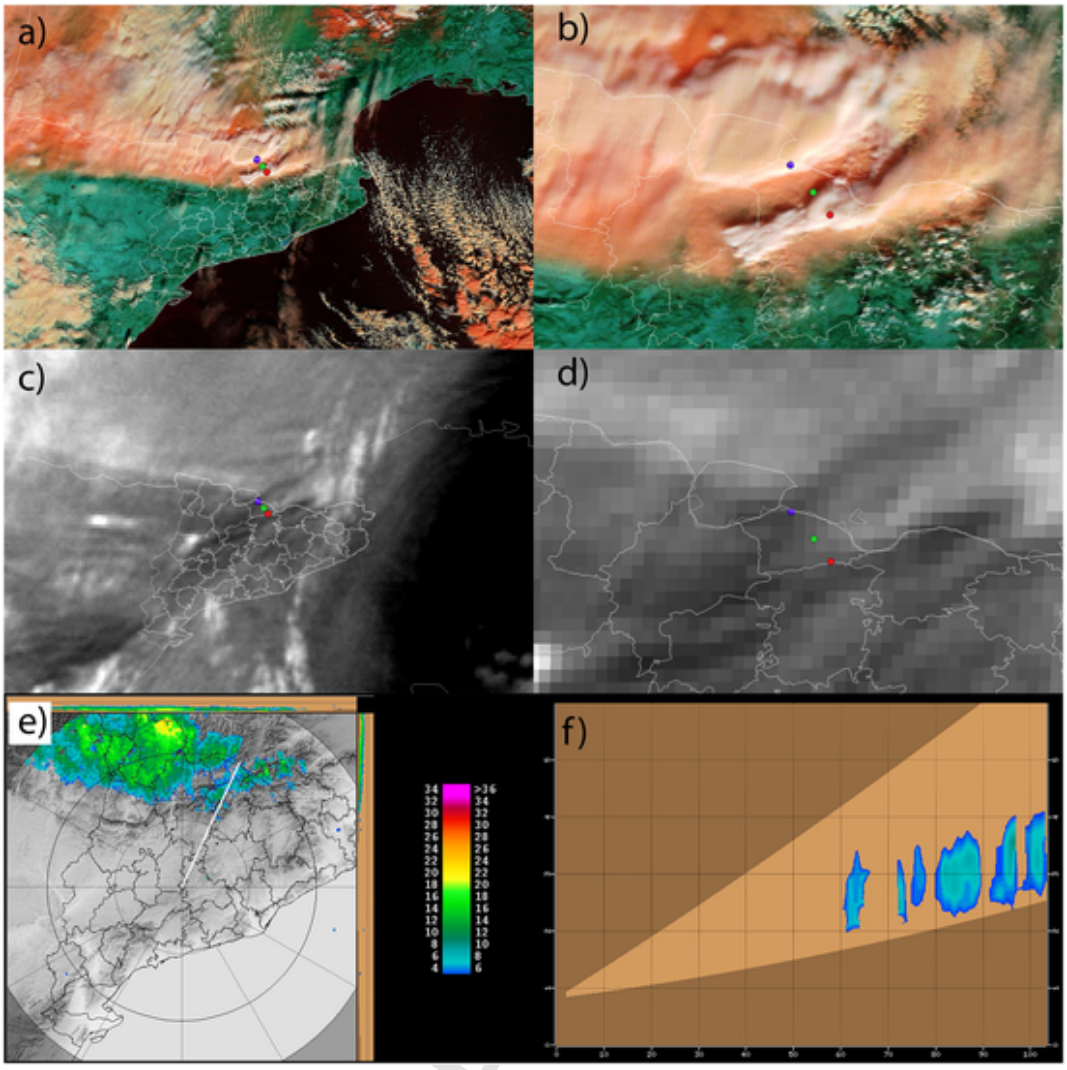

Fig. 4. (a) 1035 UTC 15 January 2017 MODIS combined band satellite image; (b) zoom over Cerdanya; (c) 1030 UTC METEOSAT water vapour channel (WV6.2) image; (d) zoom over the Cerdanya - colour dots indicate the location of Puigpedrós peak (purple), UHF wind profiler (green) and Tosa d'Alp peak (red); (e) 1030 UTC CDV weather radar maximum reflectivity field (dBZ) with a 150 km range and (f) cross section of radar reflectivity (dBZ) along the segment indicated in e). Range rings in panel (e) are plotted every 50 km and range and height in panel (f) are expressed in km. (For interpretation of the references to colour in this figure legend, the reader is referred to the web version of this article.)

one north of the Puigpedrós crest (purple dot in Fig. 4a) and another deep cloud band that starts over the location of the UHF (green dot in Fig. 4) and covers the Tosa d'Alp peak (red dot in Fig. 4a). The cloud structure reveals the presence of mountain waves over the area, with one cap cloud located at the upstream side and the next cloud band aligned with the first wave crest nearly parallel to the mountain range (zoomed in Fig. 4b).

As mountain waves favour a redistribution of water vapour mixing ratio increasing it in wave crests and decreasing it in wave troughs, satellite water vapour (WV) imagery is a good tool to explore the wave field structure (Heller et al., 2017). Fig. 4c shows the corresponding image from the WV channel of the METEOSAT satellite at 1030 UTC, where the cloud bands can also be seen over the Pyrenees. Although the horizontal resolution is poorer than in the MODIS image, parallel bands with cold and warm brightness temperatures (T_B) oriented parallel to the mountain range can be distinguished, revealing the presence of the mountain waves after the flow crossed the Pyrenees. The UHF marked location (green dot) is in a white band area, revealing low T_B, high water vapour mixing ratio, under a precipitating cloud and probably under the first updraft before the wave crest. In contrast, the Puigpedrós peak is located in a dark, high T_B band area, corresponding to the downslope flow in the immediate lee of the mountain.

We can also note that the generated lee mountain wave is not trapped far away south of the Pyrenees, and only two or three crests (troughs) are present where the water vapour mixing ratio is the highest (lowest). In addition, the evolution of the METEOSAT satellite imagery (WV, IR and VIS) reveals stationarity of the lee clouds during several hours, which is another proof of the dynamics induced by the presence of mountain waves.

The area of study is covered by the C-band Doppler weather radar network of the Meteorological Service of Catalonia (Altube et al., 2016, 2017). However, in the Pyrenees partial radar beam blockage caused by topography is not negligible which maybe a problem for stratiform precipitation typical of the cold season - see discussions in Bech et al. (2003, 2013) and Trapero et al. (2009) - so the radar observations in this area should be analysed considering this effect. Here C-band Doppler data are used to provide an overview of precipitation over the area of study - no detailed comparison is attempted with co-located MRR observations discussed later due to potential radar beam blockage and beam overshooting issues. Weather radar images from the CDV radar, the one closest to the area of study, during the

morning show precipitation over the Pyrenees extending over the south side (Fig. 4e). The radar reflectivity cross section (Fig. 4f) indicates echoes extending from 60 to 100 km from the radar reaching heights up to 4 km above sea level. In the afternoon there is no MODIS imagery available over the region of interest but the 1700 UTC WV channel image (not shown) reveals the deep cloud band located over the UHF but not the second cloud structure over the southern face as in the morning, suggesting the mountain wave would have displaced towards the north and its wavelength would have shortened as will be discussed in detail in the next sections. This interpretation is consistent with concurrent weather radar reflectivity observations(not shown) showing less extension and intensity of precipitation echoes (restricted to ranges 85 to 95 km from the radar and heights below 3.5 km).

4. Field experiment observations

In the following section we summarise the vertical structure of the atmosphere using the atmospheric sounding. Then, the ground-based instruments used in this study are explored in detail during the event in order to describe and characterise the mountain waves and the rotor positioning.

4.1. Atmospheric sounding

An in-valley atmospheric sounding (RS) was launched at 1237 UTC 15 January 2017 from the aerodrome location (point A in Fig. 1). The vertical profiles of the main magnitudes obtained with the RS are shown in Fig. 5. As the sounding was launched downstream of the mountain range, the measurements may be disturbed by the wave activity, but, as shown by Strauss et al. (2016), we can assume that above the mountain range crest line the magnitudes measured downstream would be similar than upstream of the mountain ridge. In addition, a sounding launched at Bordeaux, located 340 km northwest of the aerodrome, reveals similar wind and temperature profiles above 3000 m ASL as the in-valley aerodrome sounding.

The temperature profiles show a well mixed in-valley flow corresponding to a well mixed boundary layer (Fig. 5a, b) capped by a temperature inversion at ~2400 m AGL (~3500 m ASL) (Fig. 5a,b). In addition, there is a large positive horizontal wind shear from the surface up to 2400 m AGL, but wind speed remains nearly constant above that height (Fig. 5c). The northerly wind direction dominates the wind profile except for the lower 500 m, where it veers to the east (Fig. 5d). The squared Brunt Vaisala frequency (N^2) and the simplified Scorer pa-

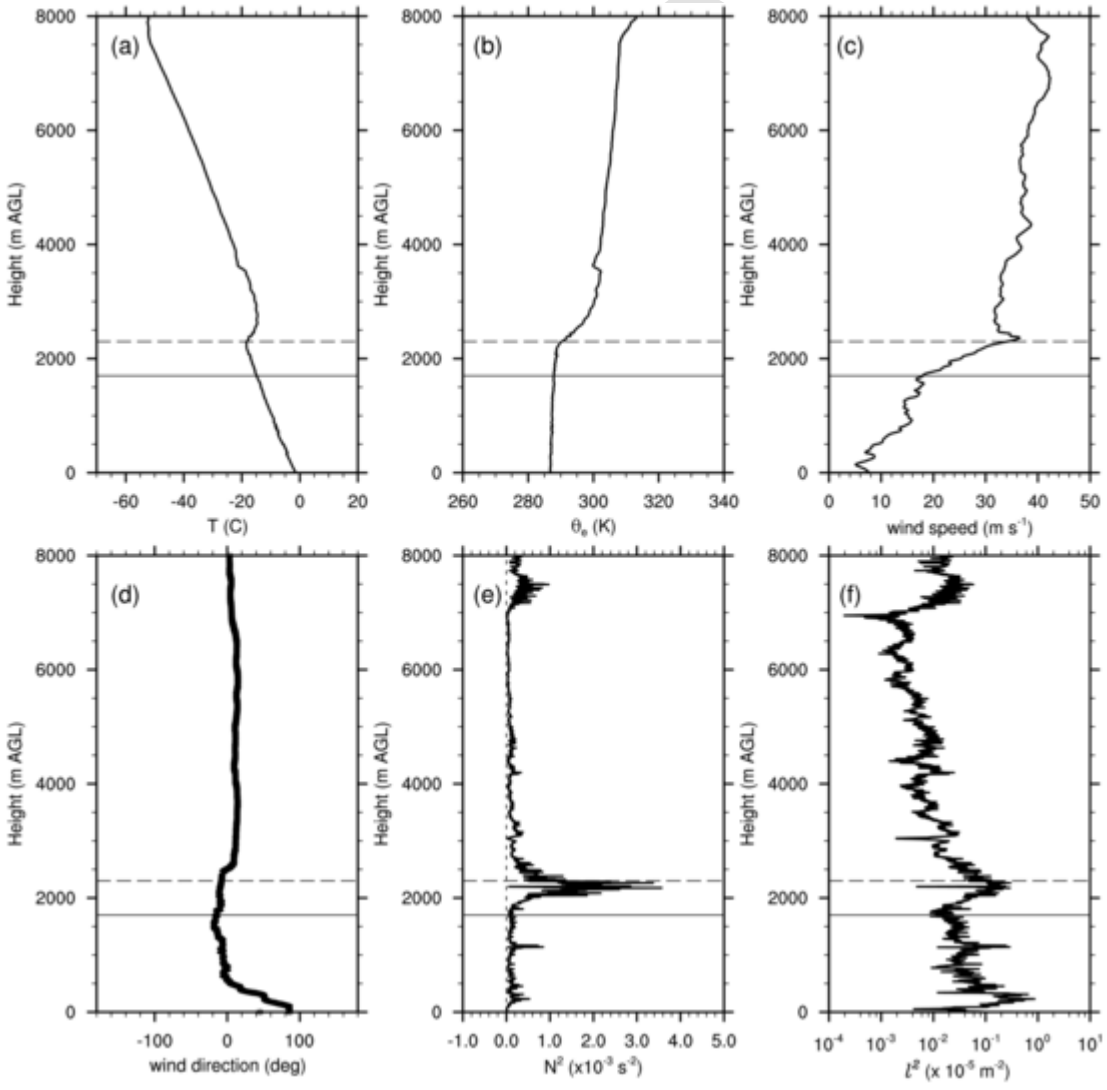

Fig. 5. Vertical profiles from the atmospheric sounding launched at 1237 UTC 15 January 2017: (a) air temperature (T), (b) equivalent potential temperature (θ_e), (c) wind speed, (d) wind direction, (e) squared Brunt-Väisälä frequency (N^2) and (f) Scorer parameter (l^2). Solid horizontal black lines mark approximately the crest line altitude (1700 m AGL or 2800 m ASL) and dashed horizontal black lines mark the base of the thermal inversion layer (2300 m AGL or 3400 m ASL).

rameter ($l^2 = N^2/U^2$) increase abruptly below the thermal inversion layer (dashed line in Figs. 5e, f), revealing strong stable conditions at these layers (Fig. 5e,f). The vertical velocity of the radiosonde decreased at these levels (not shown), as expected when the balloon crossed this stable capping layer. The thermodynamic conditions were favourable for the formation of trapped lee waves around the mountain crest level where the horizontal wind increases with height and the stability remains nearly constant, and therefore l^2 decreases with height (Scorer, 1949). However, because no lee-wave cloud train was visible on the satellite imagery, the presence of trapped lee mountain waves cannot be confirmed. In contrast, above 2400 m AGL the conditions are suitable for the development of vertically propagating mountain waves, as the horizontal wind is constant with height and the stability increases with height during several hundred meters (Durran, 2003). This is confirmed by the WV satellite imagery, evidencing that the waves reach the upper middle troposphere.

Ideally, for a northerly flow perpendicular to the Pyrenees mountain range, considering a representative topography elevation ($h_m = 2000$ m) within a stable environment ($N = 0.01\ s^{-1}$) it yields a Froude number range from 0.5 to 1 for wind speeds from 10 to 20 m s^{-1}. Within this range of values the flow is affected by non-linearity and therefore flow splitting and wave breaking can occur downstream of the mountain range. According to Smith (1989) and Vosper (2004), mountain waves and lee waves will be produced under these conditions, with chances to be accompanied by wave breaking and rotor formation. Using the parameters derived from the RS we can estimate the wave characteristics at the layers just above the mountain peaks, around 2150 m AGL. Given the potential temperature profile we approximate a simplified Scorer parameter of $l^2 = 1.27 \times 10^{-7}\ m^{-2}$, where N is the Brunt-Väisälä frequency and U is the wind speed, for a calculated $N = 0.01$ s−1 and $U = 28.7$ m $s-1$ at 2150 m AGL. Following Barry (1992), if vertical accelerations are neglected, the calculated wavelength (λ), i.e. the distance measured along the direction of propagation of the wave from the midpoint of one crest to the midpoint of the next crest can be defined as $\lambda = 2\pi/l$. Therefore, $\lambda = 17.7$ km at 2150 m AGL during the morning hours, which is approximately the distance between the two mountain ranges surrounding the Cerdanya valley, from the Puigpedrós peak to the Tosa d'Alp.

4.2. UHF wind profiler

Wind profiler observations provide the time evolution of the three wind components in a vertical air column. The vertical wind component w is a useful magnitude to determine how the wave is positioned and how it changes over height and time. As mountain waves are usually stationary, long periods with strong vertical velocities, will indicate the location of the updraft before the wave crest (for positive w) or the downdraft before the wave trough (for negative w) over the wind profiler. However, if the wave crest is located over the instrument, the vertical velocity can be zero. In addition, if the wave is not stationary and changes its horizontal wavelength or its amplitude over time then the vertical velocity will also change (Cohn et al., 2011).

As the wind profiler is located at 1077 m ASL and the mountain crest line is approximately around 2800 m ASL, the height above ground level (AGL) where the top of the mountain range is located is ~1700 m AGL. Therefore, the vertical range measurements up to 4000 m AGL are enough to capture the flow below the mountain peaks (from the surface to ~1700 m AGL) and the flow above them (above ~1700 m AGL).

Fig. 6 shows the time-height plots of the horizontal wind velocity (Fig. 6a) and the vertical wind velocity (Fig. 6b) obtained from the wind profiler for the 15 January 2017. The white spaces correspond to regions where the signal was not strong enough. The horizontal wind velocity field of the wind profiler shows a strong wind from the N-NW direction that dominates the upper levels during the whole day (Fig. 6a), which is consistent with the larger scale situation described in Section 3. In addition, there is a strong horizontal wind shear between 800 and 2000 m AGL, with the wind velocity increasing with height along the day. From the time evolution of the horizontal wind field we can distinguish three different periods. The first one covers from 0000 to 0900 UTC, strong north horizontal winds of 20 m s^{-1} prevailed at the mountain top heights (~1700 m AGL) increasing up to more than 30 m s^{-1} at 3000 m AGL. In contrast, at the bottom of the valley the horizontal wind is very weak and variable, less than 2 m s^{-1}. During the second period, from 0900 to 1600 UTC there is a wind enhancement, increasing to 30 m s^{-1} at the mountain top heights and reaching values of 40 m s^{-1} at 3000 m AGL. In addition, the wind speed increases near the valley floor, especially around 0930 UTC and around 1400 UTC, with a moderate wind speed of more than 8 m s^{-1}. The third time period starts at 1600 UTC and finishes around 2100 UTC (Figs. 6 and 7). The horizontal wind speed abruptly decreases to similar values than those on the first period of the day in a deep vertical layer with very low wind velocity from the surface up to 1200 m AGL. A detailed analysis indicates the presence of a southerly wind component appearing during 2 h, from 1700 until 1900 UTC indicating wind reversal, with opposite direction from the wind aloft, and suggesting the formation of a rotor below the mountain wave (red rectangle in Fig. 7a). The SE and S wind component appears in the layers between 150 m and 850 m AGL, therefore 700 m deep. The S counter-flow direction veers from the SE in the layers from 150 to 500 m to S from 500 to 850 m. As we will see in the next sections, the possible rotor appears to be elevated over the surface.

On the other hand, the UHF could be measuring flows advected from the surrounding and tributary valleys originated as nighttime drainage flows that transport air from the sidewall of the Cerdanya valley (Conangla et al., 2018) or similarly as in a nearby region of the French Pyrenees as described by Yus-Díez et al. (2019). In particular, La Molina valley, located southeast of the UHF (see Fig. 2a) could generate the S and SE flows, possibly favouring the counter-flow of the rotor.

The vertical wind velocity field also changed over time (Fig. 6b). During the first period, downward motions dominated the flow below the mountain top levels and intermittent updrafts were observed upper levels. Later, after 0900 UTC there is an updraft above the mountain top heights that is reinforced during the afternoon hours, i.e. 1.8 m s^{-1} at 2400 m AGL around 1400 UTC. The maximum updrafts are observed after 1600 UTC, with a maximum of 2.6 m s^{-1} at 1710 UTC at 2250 m AGL, within a deep column of upward vertical motion from 1200 to 4000 m AGL. These continuous measurements of the positive vertical velocities during the afternoon hours are indicating the location of the updraft before the first mountain wave crest over the UHF. In addition, this is the period when the horizontal wind ceases and the south horizontal wind component was observed indicating the presence of a rotor at low levels. As it will be shown in Section 5, the wind profiler may be capturing the returning part of the rotor at low levels and the updraft before the first wave crest above.

In addition, we explore the turbulent kinetic energy (TKE) dissipation rate (ε) from the UHF Doppler spectral width measurements (Jacoby-Koaly et al., 2002). This magnitude is a good measure to determine the flow turbulence intensity, and it is useful to locate spatially and temporally the turbulence within the rotor (Fig. 7b). The maximum values of ε are located at the time the rotor is formed, between 1600 and 1800 UTC, in the layers between 1000 and 1500 m AGL, at the upper part of the rotor, which is a location of the maximum turbulence similar to previous observational studies of rotors (Kuettner, 1938; Lester and Fingerhut, 1974; Strauss et al., 2015). These results are similar to those found in Doyle and Durran (2002), where

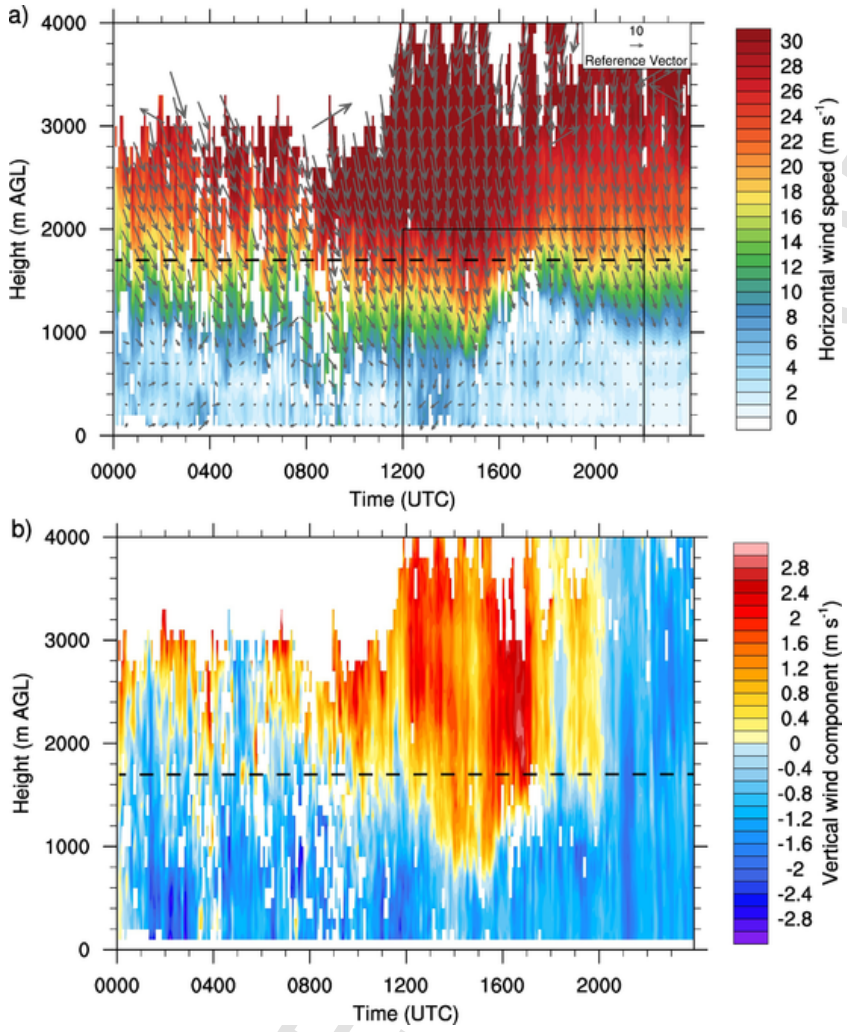

Fig. 6. Wind profiler (UHF) evolution recorded during 15 January 2017: (a) horizontal wind velocity (shaded) and horizontal wind vectors (vector); (b) vertical wind velocity. The black square in (a) corresponds to the area plotted in Fig. 7. The black dashed line corresponds to the mountain crest level. Time axis is expressed in hours and minutes UTC (hhmm).

the maximum TKE extends from the surface to the top of the rotor along the upstream edge of the first lee wave.

4.3. Micro rain radar

The MRR give us information about the vertical structure and evolution of the precipitation and the Doppler velocity of the hydrometeors above it. The evolution of the radar reflectivity above the MRR is shown in Fig. 8a. During the early morning, until 0900 UTC, relatively high reflectivity values (over 25 dBZ) with several peaks around 0500 and 0600 UTC alternated with lower values (15 to 20 dBZ). According to the Parsivel disdrometer, the particle sizes during the high reflectivity profiles had large diameters (above 10 mm) indicating strong aggregation of the snow particles. The high values of the Doppler spectrum width in the MRR data reveal increased turbulence aloft, which may provide conditions for this aggregation. After 0900 UTC, the reflectivity decreased (around 12 dBZ), and kept relatively constant until the end of the day, except for two short periods, around 0900 UTC and from 1800 to 1830 UTC, when it diminished. Interestingly, the first minimum occurs during the beginning of the morning updraft described earlier and the second minimum matches well with the possible formation of the rotor over the MRR position.

The vertical Doppler velocity is negative close to the valley surface during the whole day but becomes positive above 1000 m AGL during morning hours, from 1000 to 1300 UTC (Fig. 8b). Strong vertical velocities, i.e. values of 2.5 m s^{-1} at 2400 m AGL around 1030 UTC, suggest the location of a strong updraft during several hours over the MRR corresponding to the upstream edge of the lee wave. The Terra satellite image (Fig. 4a) confirms the location of the wave, as the edge of deep cloud band is located over the MRR at that time, where the upward moving air would enhance the cloud vertical development. As the vertical spatial distribution and the magnitudes of the vertical velocities of the MRR are similar to those derived by the UHF during the afternoon, the instruments can be capturing the same wave structure that is located over the MRR during the morning and is moved towards the UHF in the afternoon as will be explained in Section 5. Indeed, the mountain wave remains stationary for a few hours during the morning and the afternoon, but it is displaced in between. This displacement may be attributed to a shortening of the wavelength in the afternoon due to a decrease in the upstream horizontal wind speed (see Fig. 7). In the afternoon, downward motions prevail over the MRR when the rotor is generated (see Section 5). The MRR would then be pointing to the wave crest or the beginning of the downdraft just after the wave crest, in the upper layers, above ~1500 m AGL. Below this height the downward motions would correspond to the downstream part of the rotor, here revealed by falling hydrometeors observed by the MRR - see Gonzalez et al. (2019) for more details.

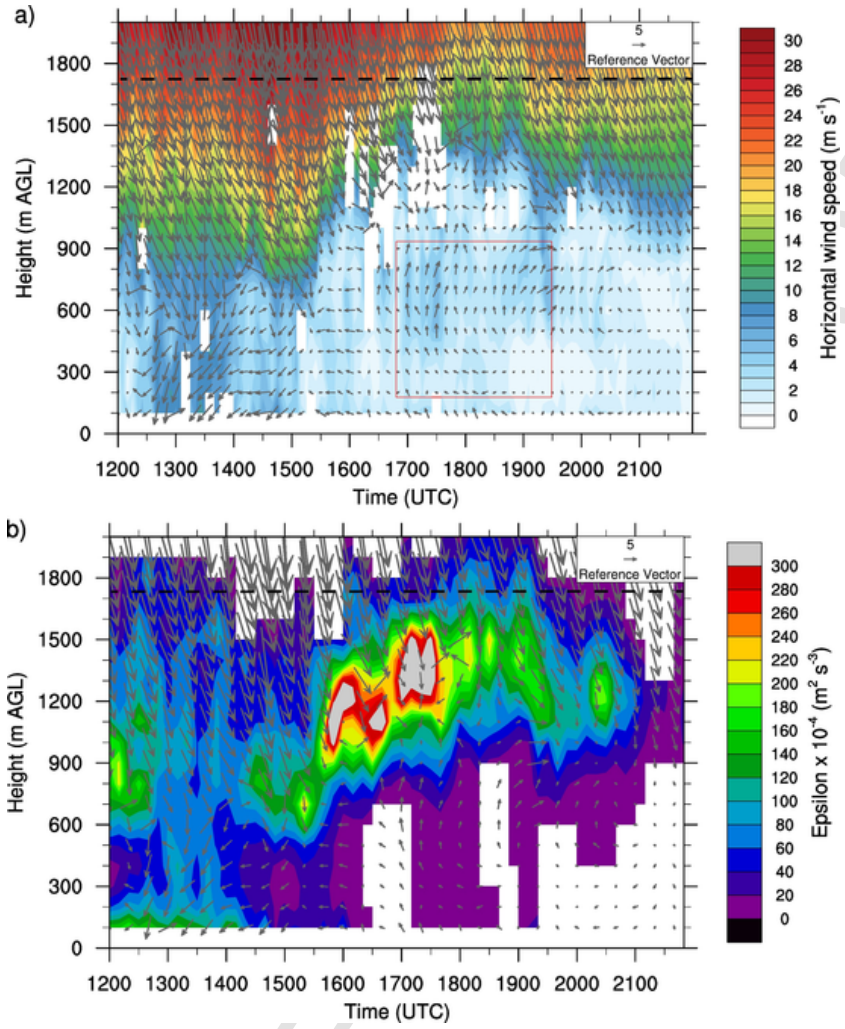

Fig. 7. Wind profiler observations from 1200 to 2300 UTC 15 January 2017 showing: (a) horizontal wind velocity (shaded), horizontal wind vectors (vector) and a red square corresponding to the lower returning part of the rotor; (b) TKE dissipation rate ε (shaded) and horizontal wind vectors (vector). The black dashed line corresponds to the mountain crest level. Time axis is expressed in hours and minutes UTC (hhmm). (For interpretation of the references to colour in this figure legend, the reader is referred to the web version of this article.)

4.4. Scanning wind Doppler lidar

LIDAR Range Height Indicator (RHI) (vertical) scans were used to explore the spatial kinematic structure of the air flow when enough backscattering particles (either solid aerosol or light precipitation particles) were present, providing line-of-sight Doppler velocity estimates. RHIs were pointing towards a 315° azimuth so that the LIDAR (located in A, see Fig. 1) scanned towards the UHF radar (at about 2.4 km), quasi-perpendicularly to the main mountain range, covering maximum heights about 1000 m AGL to explore the low-level flow characteristics corresponding to the area under the first wave crest.

Fig. 9 shows a clear southeast wind layer observed from 1701 to 1839 UTC. It is located in a layer of about 350 m thick starting about 150 m above the aerodrome ground level, therefore filling the layer between 150 and 500 m AGL. This wind layer could correspond to part of the counter-flow in the lower part of a rotor. Below this layer, a weaker northeast wind of about 1 m s^{-1} is observed. It is likely that this flow would cause the rotor to be lifted above the ground. The southeast wind is very well established being stronger from 1720 to 1759 UTC, reaching about 5 m s^{-1} at 1730 UTC. In addition, the horizontal range of the LIDAR reaches its maximum during this period, at least 2500 m ASL whereas it was less than 2000 m ASL before. This would be consistent with an increase of atmospheric aerosol content transported by the rotor when it attained its strongest intensity, without necessarily touching the ground.

4.5. Wind RASS-sodar

Observations from the Wind RASS (WR) provide information of the vertical flow structure at low layers, from the surface up to 400 m AGL at most. Wind vectors can be determined only when the acoustic backscatter intensity exceeds a certain threshold and the signal-to-noise ratio for the Doppler shift is high enough. Therefore, the vertical range of the measurements is variable and it is often shorter than 400 m (no data heights are shown as white spaces in Fig. 10).

The profile of the horizontal wind speed evolution (Fig. 10a) indicates a moderate (around 4 m s^{-1}) easterly wind at low levels during the late morning. Just before 1600 UTC the wind speed decreases over the whole column and becomes weak and variable. Most important is the southeasterly horizontal wind prevailing from 1700 to 1800 UTC, between 140 and 300 m AGL (red rectangle in Fig. 10), at the same time as the UHF wind profiler and the LIDAR measured a wind reversal zone (Fig. 7 and Fig. 9). The easterly shift between the wind measured by the WR (southeasterly wind) and by the UHF (south wind) may be due to the different location of both instruments, as the A location location 2.4 km southeast of the UHF location (see Fig. 1). As the

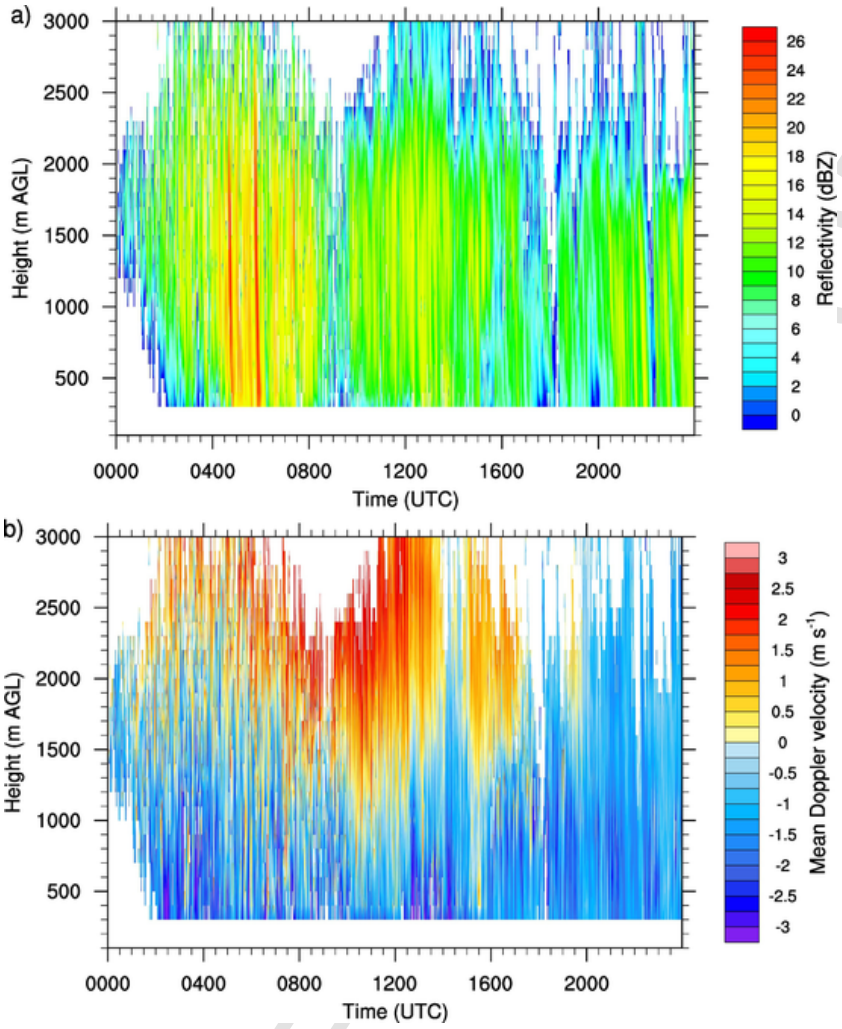

Fig. 8. Observations recorded during 15 January 2017: (a) radar reflectivity and (b) vertical Doppler velocity. In (b) positive (negative) values indicate upward (downward) motions. Time axis is expressed in hours and minutes UTC (hhmm).

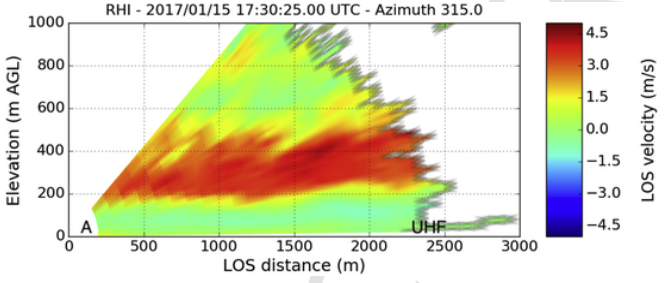

Fig. 9. Range Height Indicator (RHI) showing Line-Of-Sight (LOS) velocity in a vertical plane (azimuth 315°) pointing to the UHF direction, retrieved from the scanning wind Doppler lidar located at the aerodrome site A. Positive values (red) indicate scattering particles moving away from the LIDAR (southeast wind) and negative values (blue) mean the opposite (northwest wind). (For interpretation of the references to colour in this figure legend, the reader is referred to the web version of this article.)

rotor is usually a three-dimensional complex system evolving in time (Kühnlein et al., 2013), the structure and direction of the counter-flow may change during the event from one location to another. The evolution of the virtual potential temperature profile (Fig. 10b) reveals a stably stratified flow when the rotor is present. Very close to the surface, from 40 to 70 m, the stability is weak. Above that layer the flow is strongly stably stratified, from 70 to 200 m at 1730 UTC and from 70 to 140 m at 1800 UTC (Fig. 10c). Therefore, the temperature inversion favours that this non-turbulent flow becomes trapped in these layers, leading to a decoupling from the rotor circulation above. Therefore, WR measurements (both wind and thermal structure) confirm that the rotor circulation remains elevated from the surface around 140–200 m. In addition, WR measurements reveal intermittency of wind direction and temperature advection, which is more consistent with the rotor counter-flow rather than the La Molina valley drainage flow, which would be expected more persistent.

4.6. Surface stations

Fig. 11 shows the time evolution of the 10-m wind speed and wind direction (Fig. 11a, b) and 2-m temperature and relative humidity (Fig. 11c, d) for the automatic weather surface stations A and 8 (see locations in Fig. 1).

During the morning hours the northerly strong wind reached the valley surface, although around midday the flow turned to the east, as it is characteristic given the orientation and the shape of the valley (red dots in Fig. 11a, c). After 1600 UTC, when the elevated rotor is present, the wind at the surface turns very weak and variable, sometimes less than 1 m s^{-1}, a typical behaviour in northerly flow events observed during the Cerdanya-2017 campaign given the orientation and shape of the valley (red dots in Fig. 11a, c) After 1600 UTC, when the elevated rotor is present, the surface wind speed becomes very weak and variable, sometimes less than 1 m s^{-1}, so the wind direction is constantly

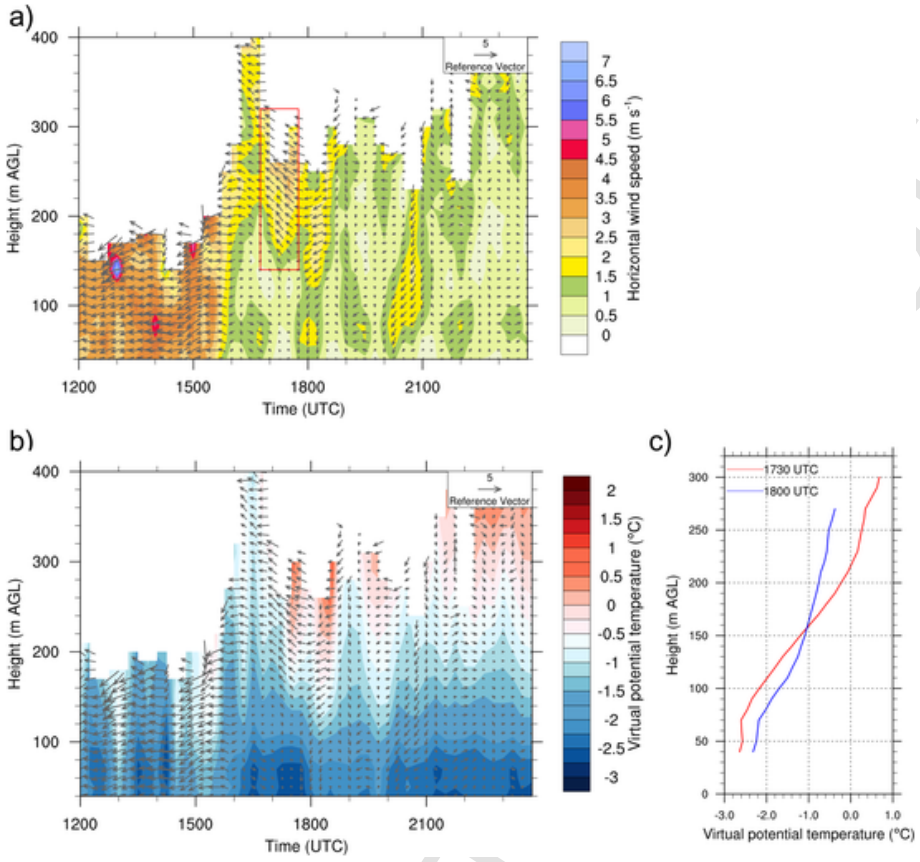

Fig. 10. Wind RASS-Sodar (WR) profile evolution for 15 January 2017 of: a) horizontal wind velocity (shaded) and horizontal wind vectors; b) virtual potential temperature (shaded) and horizontal wind vectors; c) virtual potential temperature profiles at 1730 UTC (red line) and 1800 UTC (blue line). Note that the vertical range is different from the UHF and MRR. The red rectangle in panel a) corresponds to the time where the rotor was observed by the UHF. Time axis is expressed in hours and minutes (hhmm) in panels a) and b). (For interpretation of the references to colour in this figure legend, the reader is referred to the web version of this article.)

changing (Fig. 11a, c). In addition, this matches with the sunset time, that occurred around 1650 UTC. The temperature decreased 1 degree and the relative humidity increased almost to 100% after 1600 UTC, showing the transition from daytime to nighttime and the effects of surface radiative cooling (Fig. 11b, d) combined with precipitation (see Fig. 8). As it is expected, the colder the air, the higher the relative humidity. In addition, the turbulence abruptly decreases, as indicated by the smaller fluctuation in the temperature and RH temporal series after 1600 UTC than before that hour (Fig. 11b). This is also confirmed by the evolution of the turbulent kinetic energy (TKE) from an eddy covariance station located at A (not shown).

Therefore, when the rotor is observed elevated from the surface, nighttime light and calm winds dominated the valley surface. Indeed, as confirmed by the WR measurements, the rotor circulation is decoupled around 140–200 m from near-surface stably stratified weak air flow.

5. Discussion

After the observational analysis of the measurements given in the previous sections, we are able to depict the time evolution of the general flow structure and the mountain wave and rotor positioning, summarising into two different time periods: morning and afternoon (Fig. 12).

5.1. Evolution of the mountain waves

On 15 January 2017 a northerly large scale flow arrived to the Pyrenees and produced mountain waves on its lee side. According the satellite imagery and the RS measurements the mountain waves were vertically propagated above the mountain crest. Several observations reveal the non-stationarity of the wave that was displaced from the morning to the afternoon.

During the morning, satellite imagery reveals two deep cloud bands (Fig. 4a) that were precipitating according to the surface stations and weather radar observations with higher intensity under the first cloud band, corresponding to the cap cloud formed upwind of the mountain crest. This cap cloud had the edge over the Puigpedrós peak (purple dot in Fig. 4a) where the convection was reduced, in the downward part of the mountain wave. Then, a shallow low level cloud was covering the valley with a horizontal extension about 10 km, which corresponds to the downdraft of the mountain wave before the wave trough. In terms of wave features, this distance corresponds to half the wavelength, so the wavelength can be estimated as $\lambda \sim 18$ km in the morning mountain wave (Fig. 12a). South to the wave trough, another cloud was present just above the MRR position, at the beginning of the updraft part of the wave before the first wave crest (Fig. 12a). The cloud structure, aligned in the southeast-northwest direction, had a width about 10 km covering the Tosa d'Alp peak (red dot in Fig. 4a). The first updraft before the wave crest was then located over the MRR that measured vertical velocities greater than 3 m s^{-1}, revealing a large amplitude gravity wave (Fig. 12a).

In the afternoon there was a shortening in the wavelength of the mountain wave, as a consequence of the reduced horizontal incident flow showed by the UHF measurements (Fig. 6a). Indeed, from the evolution of the vertical wind speed according to the MRR and the UHF we can infer the displacement of the wave as a consequence of the wavelength shortening in the afternoon. The first updraft before the

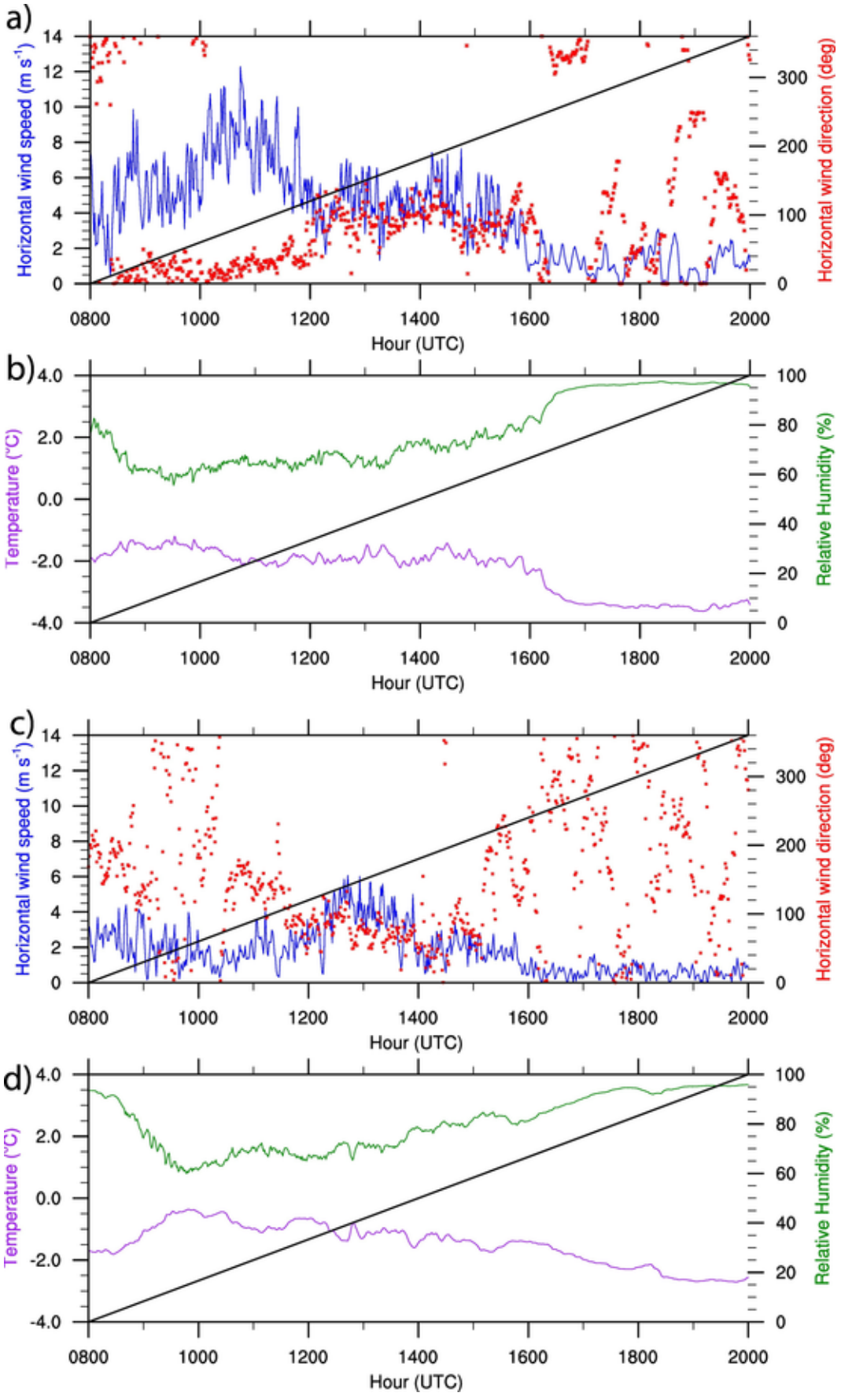
a)
Horizontal wind speed (m s-1)
Horizontal wind direction (deg)
Hour (UTC)
b)
Temperature (°C)
Relative Humidity (%)
Hour (UTC)
c)
Horizontal wind speed (m s-1)
Horizontal wind direction (deg)
Hour (UTC)
d)
Temperature (°C)
Relative Humidity (%)
Hour (UTC)

Fig. 11. Surface station measurements for the AWS located at A (a, b) and at location point 8 (c, d). Wind speed (blue line) and wind direction (red points) in (a, c) and temperature (purple line) and relative humidity (green line) in (b,d). Time axis is expressed in hours and minutes UTC (hhmm). (For interpretation of the references to colour in this figure legend, the reader is referred to the web version of this article.)

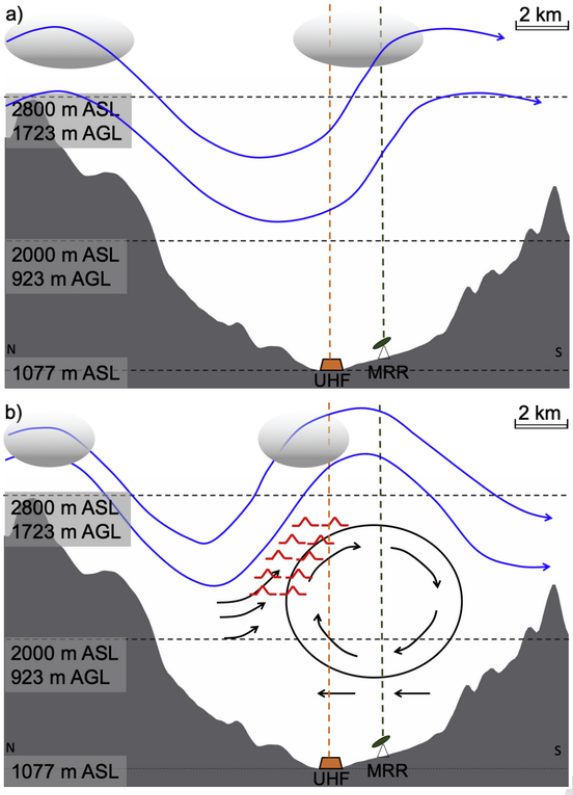

Fig. 12. Schematic representation of (a) the lee wave during the morning and (b) the lee wave and rotor location over the valley during the afternoon. Red symbols in (b) indicate the presence of moderate turbulence. The underlying terrain shape corresponds to the cross section marked in Fig. 2a, north (N) at the left and south (S) at the right, that is the cross section following the horizontal wind direction measured by the UHF at 1500 m AGL at 1700 UTC. (For interpretation of the references to colour in this figure legend, the reader is referred to the web version of this article.)

wave crest was then located over the UHF, with relatively strong vertical velocities above 1500 m AGL, similarly than observed over the MRR during the morning. Following the conceptual scheme in Fig. 12b, during the afternoon the mountain wave amplitude increased and the wavelength reduced, with an estimated length of $\lambda \sim 14$ km, when there were conditions for rotor formation underneath the mountain wave.

5.2. Rotor structure

During the morning, the gravity wave positioned as indicated in Fig. 12a did not allow the rotor to be generated because the second mountain ridge was located beneath the wave crest, as the wavelength was similar to the extension of the valley ($\lambda \sim 18$ km). Then, the valley was dominated by strong northerly winds although the first hundred meters above the ground were often disconnected from the layers above, mainly when the local circulations prevailed.

In the afternoon the rotor was formed under the wave crest, when the horizontal wind decreased and the wavelength was reduced (Fig. 12b), underneath the mountain wave, below the temperature inversion. According to the LIDAR, WR measurements and surface stations data, the rotor seemed to be elevated from the surface, with the base of the recirculating flow at around 140–200 m, because stronger stratified flow is located from the surface up to these layers. The rotor is evidenced by the southerly horizontal flow revealed by the UHF at layers between 150 and 850 m above ground, by the LIDAR vertical plan and by the WR vertical profiles only at lower layers, between 150 and 500 m AGL. According to Fig. 12b, the horizontal extension of the rotor can be approximated as a radius of 2 or 3 km, while the vertical would be shorter, a radius of 1 or 2 km. However, several smaller rotors and subrotors can be present within this big rotor as discussed in previous studies (Doyle and Durran, 2007; Doyle et al., 2009). In addition, the large TKE dissipation rate values observed over the UHF when the rotor was formed, indicate the turbulence enhancement in the area corresponding to the upstream edge of the lee wave (see red symbols in Fig. 12b), in agreement with previous research (Doyle and Durran, 2007; Cohn et al., 2011; Strauss et al., 2016). This rotor was transient, formed during a few hours, between 1700 and 1900 UTC, similar to the second case described by Kühnlein et al. (2013).

The situation during the afternoon is then similar to what is described as "transient mountain waves and rotor" in Strauss et al. (2016) (their Scenario D), but also with some features of "flow separation at a low-level valley inversion" (their Scenario B). The flow is mainly dominated by the mountain wave induced circulation but with strongly stably stratified flow near the valley bottom, from about 40 m up to 140 m, favoured by the weak and variable winds close to the surface, established over the valley during the sunset hours. In addition, the presence of the second mountain range could induce the mountain-wave circulation and the subsequent rotor (Grubišic and Stiperski, 2009). In contrast, the second ridge could have been an obstacle for the development of the rotor during the morning hours. The different depth of the rotor counter-flow between the UHF and the LIDAR data might be related to the three-dimensional structure of the rotor, which is still uncertain and cannot be inferred only using these measurements. In addition, the nighttime drainage winds from La Molina valley might influence or favour the counter-flow of the rotor, although WR measurements do not reveal a persistent outflow from this sidewall valley. A larger range of observations and model simulations would be needed in order to fully confirm the rotor positioning and the three-dimensional flow interactions, which seem more complex than the simplistic rotor models.

6. Summary and conclusions

In this work we have presented the first results of the Cerdanya-2017 field experiment focussing on the analysis of an elevated rotor associated to a mountain wave event accompanied by heavy snowfall precipitation. Measurements from instrumentation deployed in Cerdanya valley supported by satellite and radar imagery have revealed the presence of mountain waves over the valley on 15 January 2017. An associated rotor underneath the first lee wave is observed through ground based wind measurements from a UHF wind profiler, a Micro Rain Radar, a LIDAR and a Wind RASS-Sodar.

A vertically propagating mountain wave was formed over the Cerdanya valley. The continuous wind measurements have allowed to depict the evolution of the mountain wave, with greater wavelength during the morning $\lambda \sim 18$ km, and shortened during the afternoon $\lambda \sim 14$ km. This estimate was based on satellite imagery and vertical wind component data measured from the UHF wind profiler and from MRR observations in different locations. The identified rotor associated with the mountain wave was observed during 2–3 h in the afternoon when the mountain wave wavelength was shorter than in the morning and the second wave crest was aligned with the second ridge of the valley. According to the surface stations, nighttime light and calm winds dominated the surface when the rotor was formed, which could have

helped the development of the rotor circulation and kept the rotor elevated from the surface. To what extent the counter-flow of the rotor is influenced by La Molina valley outflow or other circulations is still uncertain, given the limitation of the available measurements.

The observed possible rotor had a radius of about 2 km in the horizontal, possibly a little shorter in the vertical. The most turbulent area within the rotor could be located at the upstream edge of the wave, where strong shear and TKE dissipation rate was observed. The lower part of the rotor counter-flow could be located around 140 m above the surface, above a stably stratified layer, disconnected from the surface weak flows.

Although the main features of the mountain waves and the rotor are identified, future investigation is needed in order to address the three-dimensional detailed structure of the rotor and the interaction with other flows close to the ground or from the nearby valley circulations. Indeed, the two-dimensional rotor models existing in the literature seem to be too simplistic, while real rotors are more complex and highly influenced by three-dimensional flow interactions. Numerical modelling can be a useful tool to address these issues, not only mesoscale models but also LES models in order to resolve the turbulence generated within the rotor.

Acknowledgements

The Cerdanya-2017 field campaign is a research effort organised by the University of the Balearic Islands, the University of Barcelona, METEO-FRANCE and the Meteorological Service of Catalonia. It is funded by the Spanish projects CGL2015-65627-C3-1-R, CGL2015-65627-C3-2-R (MINECO/FEDER), CGL2016-81828-REDT and RTI2018-098693-B-C32 (AEI/FEDER). We thank METEO-FRANCE/CNRM/GMEI/LISA, 4M and TRAMM teams for the data acquisition and Anna del Moral and Tiphaine Sabatier for their help processing satellite and LIDAR data respectively. We finally thank the reviewers for their constructive and exhaustive comments.

References

Adirosi, E., Baldini, L., Roberto, N., Gatlin, P., Tokay, A., 2016. Improvement of vertical profiles of raindrop size distribution from micro rain radar using 2D video disdrometer measurements. Atmos. Res. 169, 404–415.

Ágústsson, H., Ólafsson, H., 2014. Simulations of observed lee waves and rotor turbulence. Mon. Weather Rev. 142 (2), 832–849.

Altube, P., Bech, J., Argemí, O., Rigo, T., Pineda, N., 2016. Intercomparison and potential synergies of three methods for weather radar antenna pointing assessment. J. Atmos. Ocean. Technol. 33 (2), 331–343.

Altube, P., Bech, J., Argemí, O., Rigo, T., Pineda, N., Collis, S., Helmus, J., 2017. Correction of dual-PRF doppler velocity outliers in the presence of aliasing. J. Atmos. Ocean. Technol. 34 (7), 1529–1543.

Barry, R.G., 1992. Mountain, Weather and Climate. Psychology Press.

Bech, J., Codina, B., Lorente, J., Bebbington, D., 2003. The sensitivity of single polarization weather radar beam blockage correction to variability in the vertical refractivity gradient. J. Atmos. Ocean. Technol. 20 (6), 845–855.

Bech, J., Pineda, N., Rigo, T., Aran, M., 2013. Remote sensing analysis of a mediterranean thundersnow and low-altitude heavy snowfall event. Atmos. Res. 123, 305–322.

Bougeault, P., Jansa Clar, A., Benech, B., Carissimo, B., Pelon, J., Richard, E., 1990. Momentum budget over the Pyrénées: the PYREX experiment. Bull. Am. Meteorol. Soc. 71, 806–818.

Bougeault, P., Benech, B., Bessemoulin, P., Carissimo, B., Clar, A.J., Pelon, J., Petitdidier, M., Richard, E., 1997. PYREX: a summary of findings. Bull. Am. Meteorol. Soc. 78 (4), 637–650.

Bougeault, P., Binder, P., Buzzi, A., Dirks, R., Kuettner, J., Houze, R., Smith, R., Steinacker, R., Volkert, H., 2001. The MAP special observing period. Bull. Am. Meteorol. Soc. 82 (3), 433–462.

Cohn, S.A., Grubišic, V., Brown, W.O., 2011. Wind profiler observations of mountain waves and rotors during T-REX. J. Appl. Meteorol. Climatol. 50.

Conangla, L., Cuxart, J., Jiménez, M.A., Martínez-Villagrasa, D., Miró, J.R., Tabarelli, D., Zardi, D., 2018. Cold-air pool evolution in a wide Pyrenean valley. Int. J. Climatol. 38 (6), 2852–2865.

Darby, L.S., Poulos, G.S., 2006. The evolution of lee-wave-rotor activity in the lee of Pike's Peak under the influence of a cold frontal passage: implications for aircraft safety. Mon. Weather Rev. 134 (10), 2857–2876.

de la Torre, A., Pessano, H., Hierro, R., Santos, J., Llamedo, P., Alexander, P., 2015. The influence of topography on vertical velocity of air in relation to severe storms near the Southern Andes Mountains. Atmos. Res. 156, 91–101.

Doyle, J.D., Durran, D.R., 2002. The dynamics of mountain-wave-induced rotors. J. Atmos. Sci. 59 (2), 186–201.

Doyle, J.D., Durran, D.R., 2007. Rotor and subrotor dynamics in the lee of three-dimensional terrain. J. Atmos. Sci. 64 (12), 4202–4221.

Doyle, J.D., Grubišic, V., Brown, W.O., De Wekker, S.F., Dörnbrack, A., Jiang, Q., Mayor, S.D., Weissmann, M., 2009. Observations and numerical simulations of subrotor vortices during T-REX. J. Atmos. Sci. 66 (5), 1229–1249.

Durran, D.R., 2003. Lee Waves and Mountain Waves. The Encyclopedia of the Atmospheric Sciences.

Esteban, P., Jones, P.D., Martín-Vide, J., Mases, M., 2005. Atmospheric circulation patterns related to heavy snowfall days in Andorra, Pyrenees. Int. J. Climatol. 25 (3), 319–329.

Gohm, A., Mayr, G., 2004. Hydraulic aspects of föhn winds in an Alpine valley. Q. J. R. Meteorol. Soc. 130 (597), 449–480.

Gohm, A., Mayr, G.J., Fix, A., Giez, A., 2008. On the onset of bora and the formation of rotors and jumps near a mountain gap. Q. J. R. Meteorol. Soc. 134 (630), 21–46.

Gonzalez, S., Bech, J., Udina, M., Codina, B., Paci, A., Trapero, L., 2019. Decoupling between precipitation processes and mountain wave induced circulations observed with a vertically pointing k-band doppler radar. Remote Sens. 11 (9), 1034.

Grubišic, V., Lewis, J.M., 2004. Sierra Wave Project revisited: 50 years later. Bull. Am. Meteorol. Soc. 85 (8), 1127–1142.

Grubišic, V., Stiperski, I., 2009. Lee-wave resonances over double bell-shaped obstacles. J. Atmos. Sci. 66 (5), 1205–1228.

Grubišić, V., Doyle, J.D., Kuettner, J., Dirks, R., Cohn, S.A., Pan, L.L., Mobbs, S., Smith, R.B., Whiteman, C.D., Czyzyk, S., et al., 2008. The terrain-induced rotor experiment: a field campaign overview including observational highlights. Bull. Am. Meteorol. Soc. 89 (10), 1513–1533.

Guénard, V., Drobinski, P., Caccia, J., Tedeschi, G., Currier, P., 2006. Dynamics of the MAP IOP 15 severe mistral event: observations and high-resolution numerical simulations. Q. J. R. Meteorol. Soc. 132 (616), 757–777.

Heller, R., Voigt, C., Beaton, S., Dörnbrack, A., Giez, A., Kaufmann, S., Mallaun, C., Schlager, H., Wagner, J., Young, K., et al., 2017. Mountain waves modulate the water vapor distribution in the UTLS. Atmos. Chem. Phys. 17 (24).

Hertenstein, R.F., Kuettner, J.P., 2005. Rotor types associated with steep lee topography: Influence of the wind profile. Tellus A 57 (2), 117–135.

Hoinka, K.P., 1984. Observations of a mountain-wave event over the pyrenees. Tellus A 36 (4).

Hoinka, K.P., 1986. Corrigendum. Observations of a mountain-wave event over the pyrenees. Tellus A 38 (1).

Holmboe, J., Klieforth, H., 1957. Investigation of Mountain Lee Waves and the Air Flow over the Sierra Nevada. Tech. Rep.. California Univ Los Angeles.

Houze, R.A., Jr., 2012. Orographic effects on precipitating clouds. Rev. Geophys. 50 (1).

Jacoby-Koaly, S., Campistron, B., Bernard, S., Bénech, B., Ardhuin-Girard, F., Dessens, J., Dupont, E., Carissimo, B., 2002. Turbulent dissipation rate in the boundary layer via

UHF wind profiler doppler spectral width measurements. Bound.-Layer Meteorol. 103 (3), 361–389.
Jiang, Q., Doyle, J.D., Smith, R.B., 2006. Interaction between trapped waves and boundary layers. J. Atmos. Sci. 63 (2), 617–633.
Jiménez-Esteve, B., Udina, M., Soler, M., Pepin, N., Miró, J., 2018. Land use and topography influence in a complex terrain area: a high resolution mesoscale modelling study over the Eastern Pyrenees using the WRF model. Atmos. Res. 202 (Supplement C), 49–62.
Kingsmill, D.E., Persson, P.O.G., Haimov, S., Shupe, M.D., 2016. Mountain waves and orographic precipitation in a northern Colorado winter storm. Q. J. R. Meteorol. Soc. 142 (695), 836–853.
Knigge, C., Etling, D., Paci, A., Eiff, O., 2010. Laboratory experiments on mountain-induced rotors. Q. J. R. Meteorol. Soc. 136 (647), 442–450. URL. https://doi.org/10.1002/qj.564.
Kuettner, J., 1938. Moazagotl und föhnwelle (moazagotl and foehn wave). Beitr. Phys. Atmos. 1 (25), 79–114.
Kühnlein, C., Dörnbrack, A., Weissmann, M., 2013. High-resolution doppler lidar observations of transient downslope flows and rotors. Mon. Weather Rev. 141 (10), 3257–3272.
Kurz, M., 1998. Synoptic Meteorology: Second Completely Revised Edition. Deutscher Wetterdienst.
Lemus-Canovas, M., Lopez-Bustins, J.A., Trapero, L., Martin-Vide, J., 2019. Combining circulation weather types and daily precipitation modelling to derive climatic precipitation regions in the Pyrenees. Atmos. Res. 220, 181–193.
Lester, P.F., Fingerhut, W.A., 1974. Lower turbulent zones associated with mountain lee waves. J. Appl. Meteorol. 13 (1), 54–61.
Löffler-Mang, M., Joss, J., 2000. An optical disdrometer for measuring size and velocity of hydrometeors. J. Atmos. Ocean. Technol. 17 (2), 130–139.
Löffler-Mang, M., Kunz, M., Schmid, W., 1999. On the performance of a low-cost K-band Doppler radar for quantitative rain measurements. J. Atmos. Ocean. Technol. 16 (3), 379–387.
Maahn, M., Kollias, P., 2012. Improved Micro rain Radar snow measurements using Doppler spectra post-processing. Atmos. Meas. Tech. 5 (11), 2661–2673.
Markowski, P., Richardson, Y., 2011. Mesoscale Meteorology in Midlatitudes. 2. John Wiley & Sons.
Miró, J.R., Peña, J.C., Pepin, N., Sairouni, A., Aran, M., 2017. Key features of cold-air pool episodes in the northeast of the Iberian Peninsula (Cerdanya, eastern Pyrenees). Int. J. Climatol. 38 (3), 1105–1115.
Mobbs, S., Vosper, S., Sheridan, P., Cardoso, R., Burton, R., Arnold, S., Hill, M., Horlacher, V., Gadian, A., 2005. Observations of downslope winds and rotors in the Falkland islands. Q. J. R. Meteorol. Soc. 131 (605), 329–351.
Paci, A., Staquet, C., et al., 2016. The passy-2015 field experiment: atmospheric dynamics and air quality in the arve river valley. Pollut. Atmos. 231–232.
Sabatier, T., Paci, A., Canut, G., Largeron, Y., Dabas, A., Donier, J.T.D., 2018. Wintertime local Wind Dynamics from Scanning Doppler Lidar and air Quality in the Arve River Valley. Submitted to Atmosphere.
Sachsperger, J., Serafin, S., Grubišić, V., 2016. Dynamics of rotor formation in uniformly stratified two-dimensional flow over a mountain. Q. J. R. Meteorol. Soc. 142 (696), 1201–1212.
Schneider, A., Wagner, J., Söder, J., Gerding, M., Lübken, F.-J., 2017. Case study of wave breaking with high-resolution turbulence measurements with LITOS and WRF simulations. Atmos. Chem. Phys. 17 (12).
Scorer, R., 1949. Theory of waves in the lee of mountains. Q. J. R. Meteorol. Soc. 75 (323), 41–56.
Smith, R.B., 1989. Hydrostatic airflow over mountains. Adv. Geophys. 31, 1–41.
Smith, R.B., 2007. Interacting mountain waves and boundary layers. J. Atmos. Sci. 64 (2), 594–607.
Smith, R.B., Jiang, Q., Doyle, J.D., 2006. A theory of gravity wave absorption by a boundary layer. J. Atmos. Sci. 63 (2), 774–781.
Smith, R.B., Doyle, J.D., Jiang, Q., Smith, S.A., 2007. Alpine gravity waves: lessons from MAP regarding mountain wave generation and breaking. Q. J. R. Meteorol. Soc. 133 (625), 917–936.
Stiperski, I., Grubišic, V., 2011. Trapped lee wave interference in the presence of surface friction. J. Atmos. Sci. 68 (4), 918–936.
Stiperski, I., Serafin, S., Paci, A., Ágústsson, H., Belleudy, A., Calmer, R., Horvath, K., Knigge, C., Sachsperger, J., Strauss, L., et al., 2017. Water tank experiments on stratified flow over double mountain-shaped obstacles at high-Reynolds number. Atmosphere 8 (1), 13.
Strauss, L., Serafin, S., Haimov, S., Grubišić, V., 2015. Turbulence in breaking mountain waves and atmospheric rotors estimated from airborne in situ and doppler radar measurements. Q. J. R. Meteorol. Soc. 141 (693), 3207–3225.
Strauss, L., Serafin, S., Grubišić, V., 2016. Atmospheric rotors and severe turbulence in a long deep valley. J. Atmos. Sci. 73 (4), 1481–1506.
Trapero, L., Bech, J., Rigo, T., Pineda, N., Forcadell, D., 2009. Uncertainty of precipitation estimates in convective events by the meteorological service of catalonia radar network. Atmos. Res. 93 (1), 408–418.
Trapero, L., Bech, J., Duffourg, F., Esteban Vea, P., Lorente, J., 2013. Mesoscale numerical analysis of the historical November 1982 heavy precipitation event over Andorra (Eastern Pyrenees). Nat. Hazards Earth Syst. Sci. 13, 2969–2990. 2013.
Trapero, L., Bech, J., Lorente, J., 2013. Numerical modelling of heavy precipitation events over Eastern Pyrenees: analysis of orographic effects. Atmos. Res. 123, 368–383.
Tridon, F., Van Baelen, J., Pointin, Y., 2011. Aliasing in Micro rain Radar data due to strong vertical winds. Geophys. Res. Lett. 38 (2).
Udina, M., Soler, M.R., Sol, O., 2017. A modeling study of a trapped lee-wave event over the Pyrénées. Mon. Weather Rev. 145 (1), 75–96.
Valenzuela, R.A., Kingsmill, D.E., 2017. Terrain-trapped airflows and orographic rainfall along the coast of northern California. Part I: kinematic characterization using a wind profiling radar. Mon. Weather Rev. 145 (8), 2993–3008.
Valenzuela, R.A., Kingsmill, D.E., 2018. Terrain-trapped airflows and orographic rainfall along the coast of northern California. Part II: horizontal and vertical structures observed by a scanning doppler radar. Mon. Weather Rev. 146 (8), 2381–2402.
Vosper, S., 2004. Inversion effects on mountain lee waves. Q. J. R. Meteorol. Soc. 130 (600), 1723–1748.
Worthington, R., 2017. The atmosphere under the waves: forgotten meteorology from Nazi Germany. Weather 72 (8), 226–233.
Yus-Díez, J., Udina, M., Soler, M.R., Lothon, M., Nilsson, E., Bech, J., Sun, J., 2019. Nocturnal boundary layer turbulence regimes analysis during the bllast campaign. Atmos. Chem. Phys. 19 (14), 9495–9514.